

REMOTE SENSING OF TROPICAL CYCLONES

Observations from *CloudSat* and A-Train Profilers

BY NATALIE TOURVILLE, GRAEME STEPHENS, MARK DeMARIA, AND DEBORAH VANE

A collection of *CloudSat* and A-Train satellite observations, model data, and storm-specific information compiled from overpasses of tropical cyclones.

Satellite imagery of TCs (see the appendix) has changed the way we monitor and study these major storm systems. These storms are routinely monitored by operational meteorological satellites, providing practically continuous surveillance of TCs since the mid-1960s (Kidder and Vonder Haar 1995). Although these spaceborne observations have improved the surveillance of the movement and intensity of these storms, large-scale information about the internal structure of these storms and reliable estimates of their destructive power using the same spaceborne observations have proven to be much more elusive.

Intensity and location estimates derived from the Dvorak technique (Dvorak 1972, 1975, 1984) were developed from examination of satellite imagery of TCs and presently serve as the foundation of best-track estimates for the NHC, JTWC, and CPHC. Maximum sustained wind, defined as the 1-min average wind speed at an altitude of 10 m, is widely used to characterize the intensity of TCs and, thus, the potential for damage to property and life. It has proven to be difficult, however, to relate this measure of storm intensity to existing satellite radiometric quantities (see Luo et al. 2008 for review). Furthermore, the important influence of internal physical properties (e.g., ice microphysics) on the gross characteristics of the storm intensity and motion has recently become appreciated (Camp and Montgomery 2001; Houze et al. 2006; Jin et al. 2014). Realistic representation of clouds and precipitation in TCs is particularly important for accurate representation in numerical and dynamical models to make forecasts as accurate as possible.

With the launch of *CloudSat* (CS), a new tool became available to study the internal properties and structure of TCs. The CS CPR provides a measurement of W-band (94 GHz) radar reflectivity versus altitude in a nadir slice along the satellite track. The 3-mm-wavelength CPR has a minimum reflectivity of -30 dBZ with a 70-dB dynamical range and vertically samples every 240 m between the surface and

AFFILIATIONS: TOURVILLE—Cooperative Institute for Research in the Atmosphere, Colorado State University, Fort Collins, Colorado; STEPHENS AND VANE—Jet Propulsion Laboratory, Pasadena, California; DeMARIA—Technology and Science Branch, National Hurricane Center, Miami, Florida

CORRESPONDING AUTHOR: Natalie Tourville, Cooperative Institute for Research in the Atmosphere, Colorado State University, 1375 Campus Delivery, Fort Collins, CO 80523-1375
E-mail: natalie.tourville@colostate.edu

The abstract for this article can be found in this issue, following the table of contents.

DOI:10.1175/BAMS-D-13-00282.1

In final form 27 October 2014
©2015 American Meteorological Society

30 km for 125 vertical bins. With a footprint size of 1.4 km × 1.7 km, CS repeats the same ground track every 16 days and completes 14 equator overpasses on a daily basis. The CS CPR excels in detection of condensed cloud water, ice and light precipitation (Ellis et al. 2009), cloud-layering structure (Mace et al. 2009), and quantitative information about the distribution of liquid and ice hydrometeors (Stephens et al. 2008). CS observations have played an important role in redefining the global distribution of cirrus clouds and deep convection (Sassen et al. 2009). Accurate representation of clouds is essential in understanding Earth's energy balance and distribution of heating. Revised estimates of the global mean energy balance reveal larger longwave radiation received on Earth's surface and more precipitation generated globally (Haynes et al. 2013; Stephens et al. 2012).

CS joined the A-Train in 2006, an international series of Earth-observing satellites 705 km above Earth's surface (Stephens et al. 2002). The A-Train satellite constellation provides active and passive atmospheric measurements at microwave, infrared, and optical wavelengths following nearly identical ground-track footprints (Fig. 1). The A-Train satellites fly in a sun-synchronous, circular orbit

overpassing the equator at 1330 UTC local time. The satellite *Aqua* contains the following instruments used in this dataset: AIRS, AMSR-E, CERES, MODIS, and the satellite *CALIPSO*, containing the CALIOP instrument. After a battery anomaly on 17 April 2011, CS resumed daylight-only observations on 27 October 2011, rejoined the A-Train on 15 May 2012, and maneuvered to achieve overlap with CALIOP observations on 18 July 2012. Daylight-only observations limit the number of possible observations to around half the observations pre-battery anomaly (Nayak et al. 2012). CS flies 17.5 s ahead of *CALIPSO* (post-battery anomaly CS flies 103 s behind *CALIPSO*) and 150 s behind *Aqua* (post-battery anomaly 176 s behind *Aqua*). This combined set of observations from multiple instruments allows for nearly simultaneous observations of globally complex storm systems.

While passes of the nadir-pointing CPR antenna over TCs occur infrequently in comparison to the much denser sampling of clouds and precipitation, they do happen enough to provide compilations of data that can uniquely serve the research community for examining storm structure and its variation as a function of, for example, the surrounding

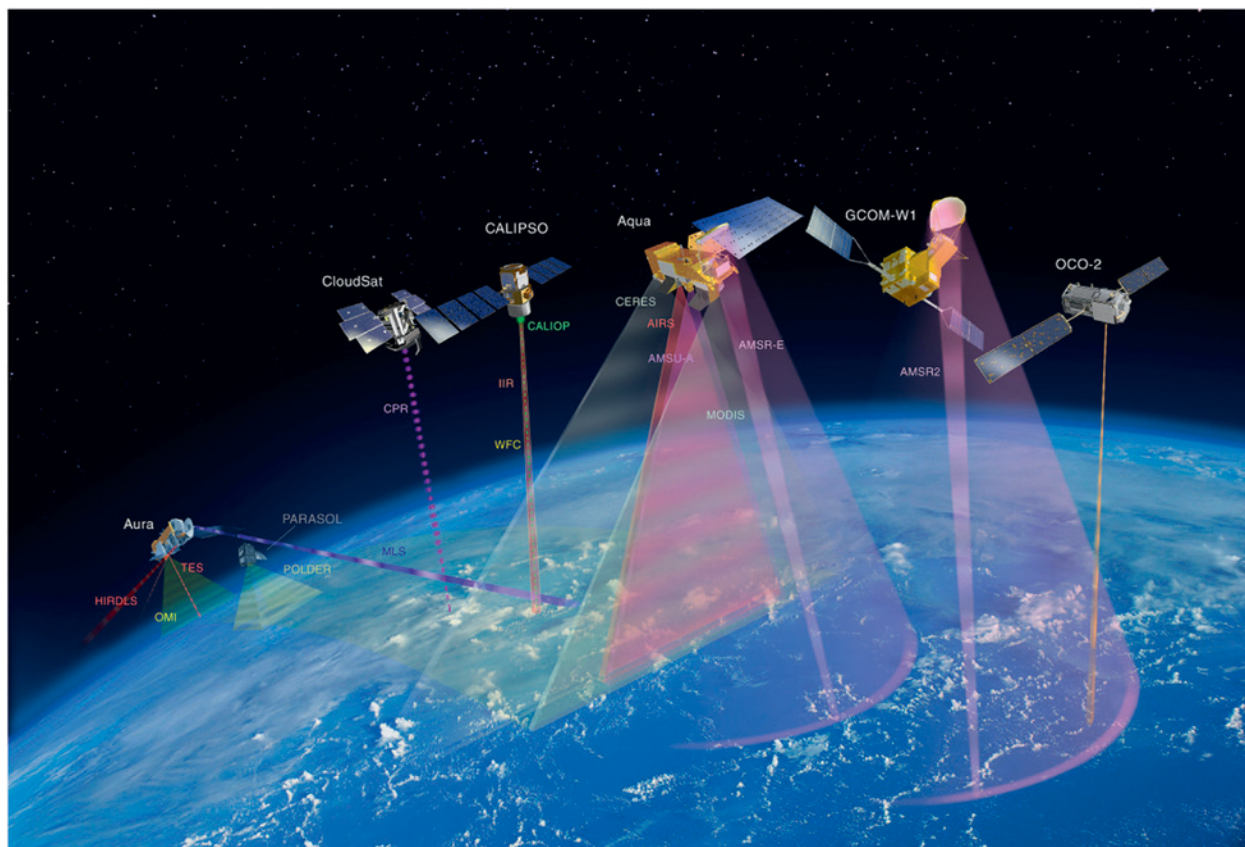


FIG. 1. A-Train constellation of satellites.

environment. This paper describes the dataset of TC overpasses profiled by CS with corresponding data obtained from complementary A-Train sensors along with select model data. A description of the dataset archived at the CS DPC (Stephens et al. 2008) and the data can be downloaded from the CS DPC (www.cloudsat.cira.colostate.edu/). Figure 2 provides a sense of the volume of TC data contained at the DPC. This is a composite of all storms intersected by the CPR (during the period June 2006–December 2013) and indicates the number of TC radar profiles as a function of radial distance from storm center. The number of profiles peaks at 875 km from storm center and decreases, as the horizontal span of a TC and the interacting environment infrequently spans larger than this size. Over 10 million TC radar profiles have been collected by the CS CPR, including over 170,000 TC profiles inside 100 km of storm center.

The motivation behind this study is to present the A-Train and CS TC dataset to the research community, as vertical observations of TCs provide a valuable research opportunity. We illustrate the value of this dataset by examining the environmental condition, the vertical wind shear, which exerts an important influence on the intensity and structure of TCs and is considered a significant parameter in observational TC forecasting. Examining the effects of vertical wind shear on TCs has mostly been achieved from a numerical modeling perspective with observations

limited to aircraft reconnaissance and passive satellite measurements.

DATASET DETAILS. The dataset is constructed from CS CPR intercepts of TCs within 1000 km of the storm center. For each CS overpass of a TC, an HDF-EOS file is created containing CS reflectivity, corresponding CS level-2 products, and derived model data from NOGAPS data (version 4.0) and ECMWF (Uppala et al. 2005). NOGAPS¹ is a global, spectral forecast model with a spatial resolution of 0.5° (~54 km) and provides useful thermodynamical fields to determine temperature, melting layer, and precipitation structures (Hogan and Rosmond 1991). Best-track storm-specific information is provided from the ATCF by observations from the JTWC, CPHC, and NHC (Sampson and Schrader 2000). Latitude, longitude, maximum sustained 1-min wind speed, and minimum pressure are linearly interpolated from 6-hourly storm positions. GFS wind shear (difference in wind speed/direction at 200 and 850 hPa) (EMC 2003) and Reynolds SST (Reynolds et al. 2007) sampled at storm center are also included for each TC storm intercept. A complete listing of all data sources and variables for each TC overpass is provided in Table 1. Each HDF-EOS file format is labeled corresponding to the storm name,

¹ NOGAPS is now NAVGEM.

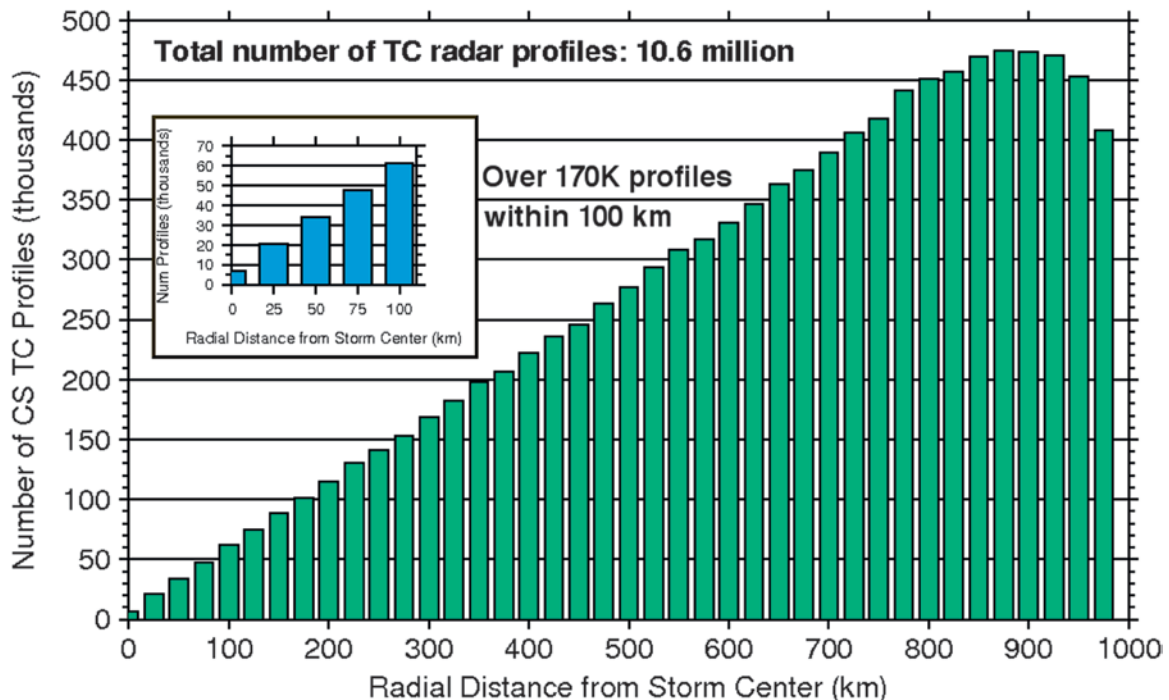


FIG. 2. Number of CPR profiles as a function of radial distance from the center of the TC as defined by best-track data for the period 2 Jun 2006–31 Dec 2013.

basin location, CS granule, and date of overpass—for example, 2009256031109_17967_CS_TC-WPAC-15W_CHOI-WAN_GRANULE.hdf. The naming convention is described as follows: 2009 is the TC year; 256 is the day of the year; 031109 is the hour (03), minute (11), and second (09) of the start of the CS overpass; 17967 is the CS granule number; TC-WPAC-15W describes the basin, WPAC, and the storm identifier (15W); and CHOI-WAN is the WMO name.

A special subset of CS TC observations is collocated to additional satellite instruments and global model data for the period May 2008–April 2010. This dataset, known as the YOTC, aims to provide a realistic representation of tropical convection with high-resolution satellite observations and operational model datasets (Waliser et al. 2012). Approximately 2,808 CS TC overpasses include additional quantities from CALIPSO, MLS, AIRS, AMSR-E, CERES, MODIS, and specialized YOTC analysis from ECMWF.

The Satellite Meteorological Applications Section at NRL processes CS data as part of its extensive real-time TC satellite processing. Prior to the CS battery anomaly, overlays of CPR profiles of TCs are

generated onto corresponding *Aqua* sensors (MODIS and AMSR-E) and geostationary satellites (Mitrescu et al. 2008). In addition to the HDF-EOS data file for each TC overpass, these satellite and CS CPR overlays are provided as a visual subset (if available). These satellite overlays provide a two-dimensional horizontal cloud structure with a corresponding CS track superimposed on top of the satellite imagery. Figures 3 and 4 represent examples of this type of imagery. The combination of satellite visible and/or infrared images with three-dimensional cross sections of CS CPR intersects provides an easy way to visually represent the CS overpass in relation to the TC.

Statistics of the dataset are detailed in Tables 2 and 3. All CS overpasses within 1000 km of storm are sorted by basin and year. The WPAC basin region contains the greatest number of TC CPR intercepts followed by the SHEM, ATL, EPAC, CPAC, and IO regions. The CS CPR has intersected 7,941 TC systems during the period 2 June 2006–31 December 2013 and intersected every named global TC prior to the battery anomaly in April 2011. A TD is defined as containing winds less than or equal to 17 m s^{-1} , a TS contains winds between 18 and 32 m s^{-1} , and an HTC-strength

TABLE 1. Summary of data sources and parameters for each TC overpass.

Data source	Description	Parameters
AMSR-E	AMSR-E levels 2A and 2B matched to the CS footprint	Rain rates, water vapor, wind speed, SST, liquid water path, 89H BT
CS 2B-GEOPROF	Cloud geometric profile product	CPR reflectivity, cloud height, and cloud mask
CS 2B-GEOPROF-lidar	2B-GEOPROF and CALIOP lidar-correlated observations	Cloud fraction, hydrometeor layer base and top for up to five layers
CS 2B-CLDCLASS	Eight types of clouds	Cloud classification
CS 2B-CWC	CS cloud and IWC	IWC, IWP, ice effective radius, ice number concentration
CS 2C-RAIN-PROFILE and CS 2C-PRECIP-COLUMN	Estimate of surface precipitation from CS CPR reflectivity profiles and temperature and humidity data from ECMWF auxiliary dataset	Precipitation rates, type of precipitation, freezing level, highest and lowest cloud layers, SST, rain-top height, frozen precipitation height, convective or stratiform precipitation types
CS 2B-FLXHR	Flux and heating rates from estimates of ice and water content	Heating rates inferred from upwelling and downwelling longwave and shortwave aux profiles
CS 2B-TAU	Cloud optical properties	Total cloud optical depth and mean effective radius
CS MOD-AUX	MODIS products matched to the CS footprint	Brightness temperature, cloud-top pressure, CTT, and CTH
NoGAPS	0.5° ($\sim 54 \text{ km}$)-resolution global model fields	Temperature, dewpoint, and height at 17 pressure levels; SST; surface air temperature; U and V wind speeds
CS ECMWF-AUX	ECMWF data sampled along CS track	Pressure, 2-m temperature, specific humidity
Storm-specific information	Best track from NHC/JTWC, Reynolds storm center SST, and GFS wind shear	Best-track storm latitude, longitude, wind speed, pressure, Reynolds SST, GFS wind shear (200–850 hPa)

storm contains winds greater than 33 m s^{-1} . More importantly, CS has intersected 1,120 HTC-strength storms with 112 of these overpasses within 100 km of storm center.

The dataset is available to the science community and can be downloaded from the CS DPC (www.cloudsat.cira.colostate.edu/). Registration to access the data is free. The dataset will be updated with preliminary TC overpass data corresponding with the release of CS data products. ATCF best-track information for each TC is considered preliminary until official best-track information is released (after the end of each TC season).

DATA EXAMPLES.

Typhoon Choi-Wan. The first illustration of a CS TC overpass is of Typhoon Choi-Wan, which is one of the strongest TCs CS has fully intersected. This storm formed in the WPAC on 12 September 2009, 470 mi east of Guam. Favorable upper-level dynamics and ocean heat content quickly allowed Choi-Wan to intensify into a typhoon on 13 September 2009. The CSCPR completed an ascending southeast-to-northwest overpass of the

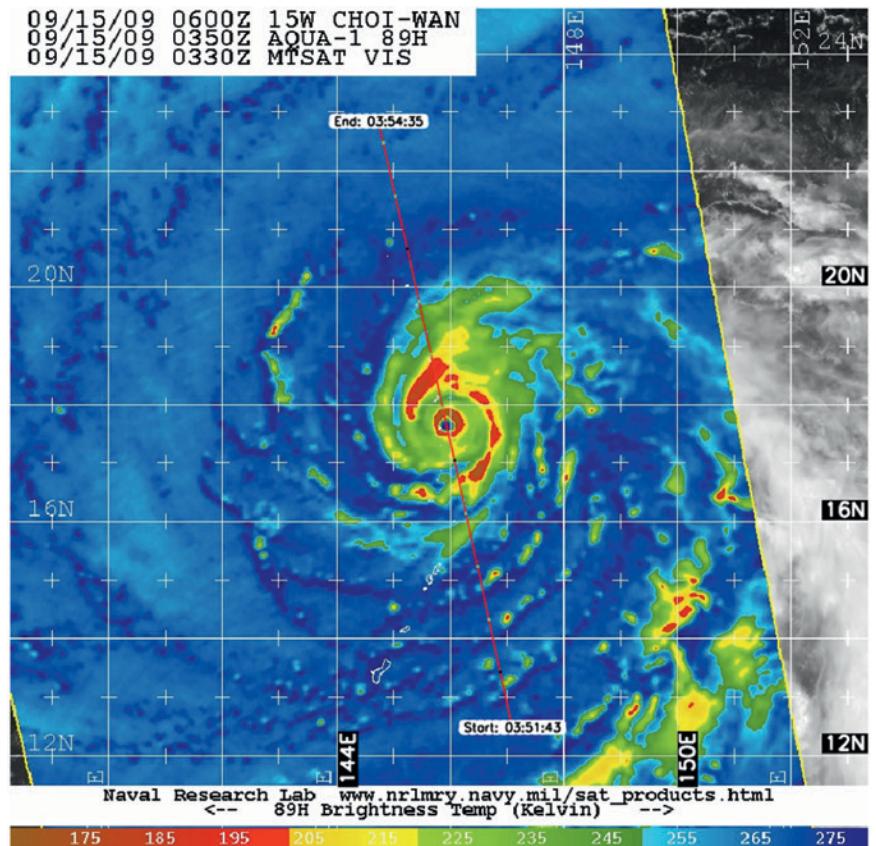
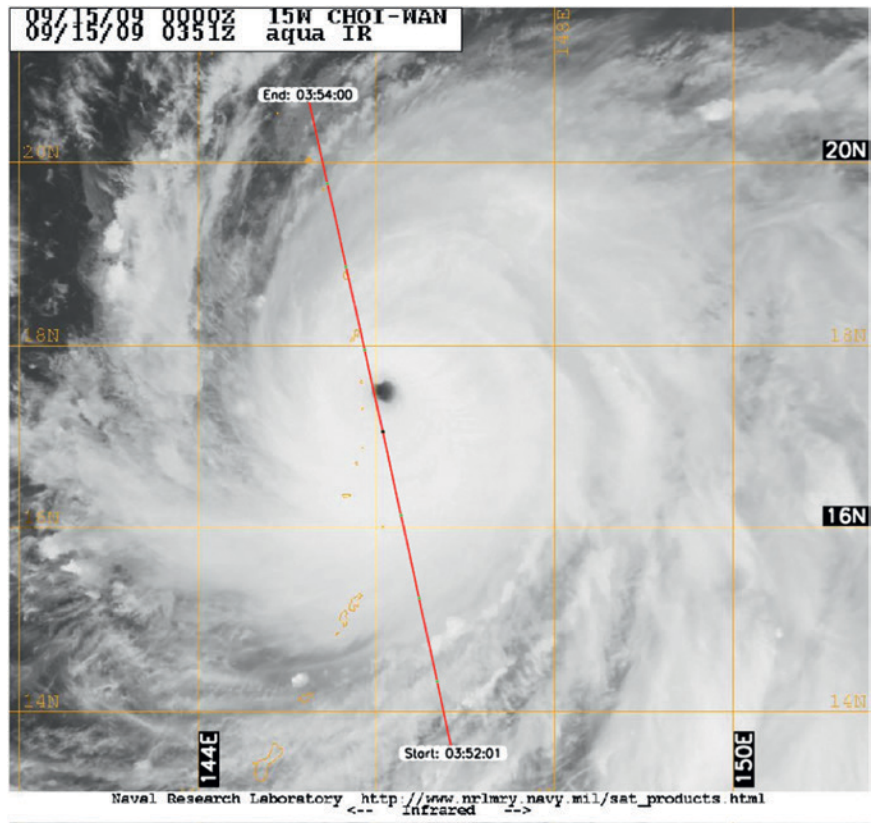


FIG. 3 (TOP). Aqua infrared imagery overlaid with the CS trajectory through Typhoon Choi-Wan on 0352 UTC 15 Sep 2009. (Image courtesy of NRL.)

FIG. 4 (BOTTOM). AMSR-E imagery overlaid with the CS trajectory through Typhoon Choi-Wan on 0352 UTC 15 Sep 2009. (Image courtesy of NRL.)

system on 0350 UTC 15 September with maximum sustained 1-min winds of 145 mph and 926-hPa minimum pressure. This is one of a few instances (approximately 33 cases in all) where the CS CPR has intersected the eye (defined within 25 km of storm center) of an HTC-strength storm. The eye of Typhoon Choi-Wan is clearly visible from the corresponding MODIS (Fig. 3) and AMSR-E (Fig. 4) imagery. The cross section starts at 0351:43 UTC with a starting distance of 0 km and travels north-westward through the storm ending at 0354:35 UTC (Figs. 3 and 4). The MODIS imagery overlaid with the corresponding CS track provides a useful overview of the visible cloud structure (Fig. 3). The AMSR-E 89-GHz imagery reveals the cold temperatures of deep convection and ice precipitation at the higher levels of the storm system using the color scheme of red against the blue ocean background (Fig. 4). The eye is largely cloud free with a concentric closed ring of eyewall convection surrounding

the area. IWC and reflectivity profiles from the CS vertical cross section are shown in Figs. 5a and 5b, respectively. Large amounts of IWC are found in the inner eyewall region and in areas farther from the storm (at points 800 and 1,000 in the cross-track distance). IWC plays an important role, yet not well understood, in TC development through the release of latent heating and precipitation production. Ice water path (an integrated measurement of IWC) is 10 kg m^{-2} in the northern section of the eyewall. The reflectivity profile and cloud properties (Fig. 5b) show higher values (bright orange and red bands of 10 and 15 dbZ, respectively) over 16 km in height near the eyewall. CTH gradually decreases as the distance from the storm center increases. Frozen precipitation height values generally follow the height of the deeper convective cores (red) and the freezing level is a consistent 5 km (Fig. 5b). The freezing level, where precipitation changes from liquid to frozen particles, attenuates the CPR signal below this level in

areas of moderate-to-heavy precipitation. CTT, MODIS $11\text{-}\mu\text{m}$ temperature, AMSR-E 89-GHz temperature, and NOGAPS surface temperature are plotted in Fig. 5c. The AMSR-E 89-GHz temperature signal detects a cold cloud top in the northern eyewall section of 120 K, indicating large amounts of ice in the upper levels of the system and corresponding to the higher amounts of IWC detected by the CPR. The MODIS $11\text{-}\mu\text{m}$ signal increases in temperature in the eye region as it detects the surface of the ocean from the cloud-free eye. NOGAPS surface temperature and SST from AMSR-E, NOGAPS, and ECMWF (all overlaid on top of each other) (Fig. 5d) are consistent along the CS track. Precipitation estimates from CS (Fig. 5d) show the limitations of CS as precipitation radar in heavy precipitation but performs well in lighter precipitation

TABLE 2. Total number of TC CS overpasses by basin and season within 1000 km of storm center.

Year	WPAC	EPAC/CPAC	ATL	SHEM ^a	10	Total
2006 ^b	413	352	152	—	23	940
2007	398	209	238	403	94	1,342
2008	376	309	363	478	111	1,637
2009	446	290	156	400	60	1,352
2010	241	130	329	266	78	1,044
2011 ^c	30	7	0	260	10	307
2012 ^c	197	105	177	137	27	643
2013 ^c	201	143	78	207	28	657
2014 ^c	—	—	—	19	—	19
Total	2,302	1,545	1,493	2,170	431	7,941

^a Southern Hemisphere storm season is from June to July.

^b CPR began taking observations on 2 Jun 2006.

^c CS experienced a battery anomaly on 17 Apr 2011 and resumed daylight-only observations on 27 Oct 2011. The remaining overpasses are based on CPR overpasses during daylight-only observations.

TABLE 3. CS overpasses of TD, TS, and HTC by radial distance from storm center.

	$\leq 10 \text{ km}$	$\leq 25 \text{ km}$	$\leq 50 \text{ km}$	$\leq 100 \text{ km}$	$\leq 250 \text{ km}$	$\leq 500 \text{ km}$	$\leq 1,000 \text{ km}$
TD	33	101	210	426	1,092	2,192	4,605
TS	17	58	103	219	553	1,062	2,216
HTC	12	33	67	112	263	540	1,120
Total	62	192	380	757	1,908	3,794	7,941

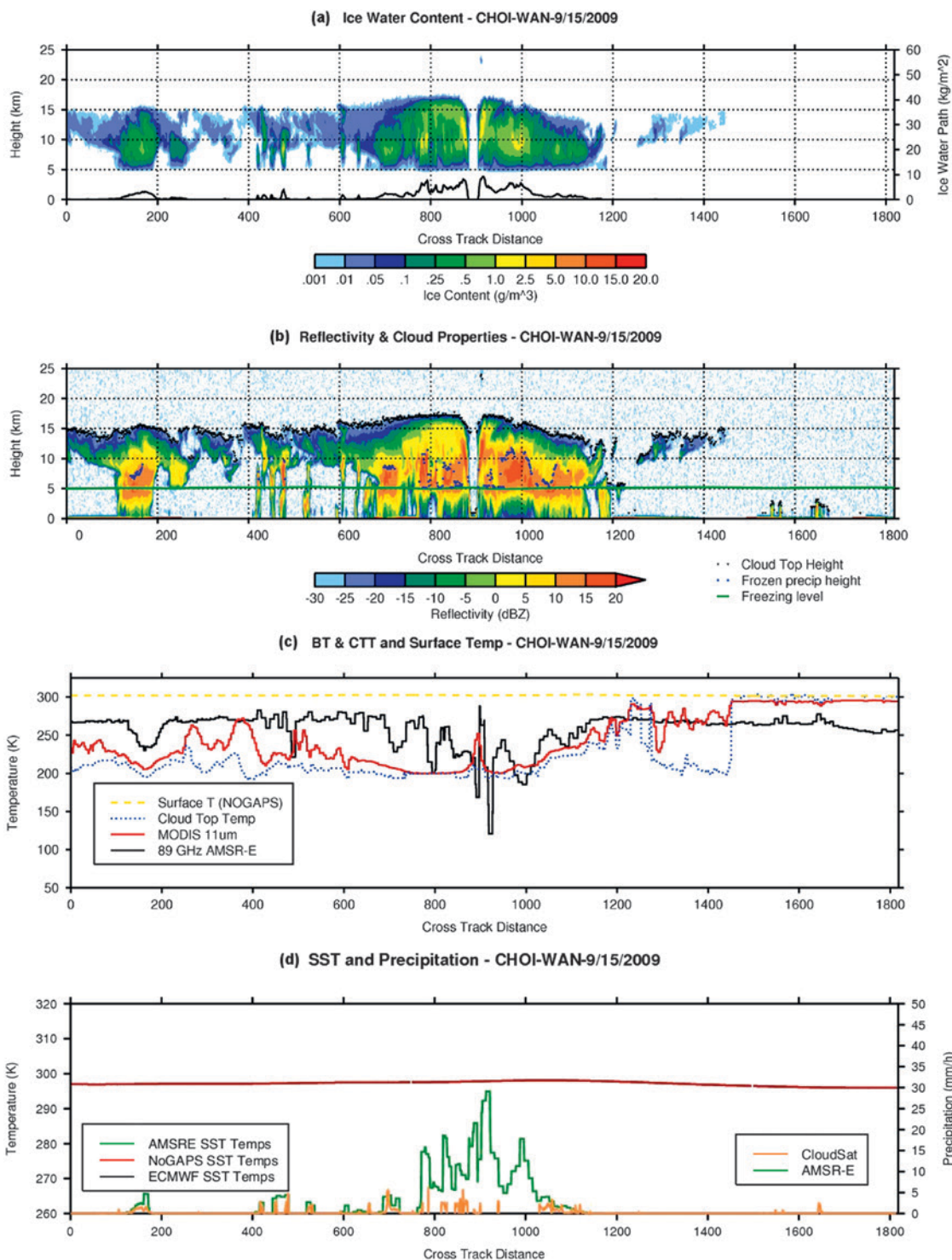


FIG. 5. (a) CS IWC and IWP; (b) CS reflectivity, frozen precipitation height, MODIS CTH, and freezing level; (c) NOGAPS surface temperature, CTT, MODIS 11-mm temperature, and AMSR-E 89-GHz brightness temperature; (d) SST (NOGAPS, ECMWF, AMSR-E) and precipitation (CS and AMSR-E) of Typhoon Choi-Wan on 0352 UTC 15 Sep 2009.

areas away from the core storm system. AMSR-E detects precipitation rates of close to 30 mm h^{-1} in regions of the northern eyewall section.

CS cloud classification (2B-CLDCLASS product) identifies mostly deep convection cloud types with stratus at the base of the eye center and scattered

outside the areas of deep convection (Fig. 6). Areas of altostratus and cirrus surround the convective rainbands with a thick cirrus canopy in the upper troposphere, engulfing a majority of the storm system.

A close-up view of the eye of Typhoon Choi-Wan is shown in Fig. 7a with a one-to-one zoomed-in relationship of the eye area shown in Fig. 7b. This close-up view of the eye clearly shows the slope of the eyewall at 45° and reveals details of the cloud structure at the top of the storm and an enhanced view of the northern eyewall hot tower. Hot towers are theorized to occur with rapid TC intensification (Riehl and Malkus 1958; Montgomery et al. 2006; Guimond et al. 2010); as was the case with Typhoon Choi-Wan, the storm intensified by 25 kt (12.75 m s^{-1}) in 18 h previous to the CS CPR overpass (according to JTWC best-track storm information). It is theorized that the undiluted cores rapidly ascended to the top of the storm from vigorous updrafts by deep convection. Large amounts of latent heat are released during this process as water vapor condenses and freezes quickly into ice. The zoomed-in portion of Fig. 7b details the core of the northern hot tower at 10-km height containing a CS reflectivity value of over 20 dBZ.

REFLECTIVITY STRATIFICATIONS ACROSS VARYING WIND SHEAR.

With the volume of data collected, it is possible to composite TC structure information with respect to various environmental parameters that are known to have a controlling influence on storms. To illustrate this characteristic of the data, we show composites of the vertical structure of TCs as a function of environmental wind shear. Wind shear plays a critical role in TC dynamics and formation, especially evolution of internal structure and storm dynamics as well as the storm's interaction with the surrounding environment (DeMaria 1996; Frank and Ritchie 2001; Knaff et al. 2004). Many studies have been published on radius-versus-height structure using aircraft observations (Barnes et al. 1983; Black et al. 2002; Houze et al. 2006; among others). These studies provide an important framework

and foundation in understanding TC intensity change and interactions between inner-core areas and outer rainbands. The dynamics of the internal structure and interactions with the storm environment, especially wind shear, are poorly resolved by numerical models placing a high importance on observations of TCs. Over the last decade, with the introduction of satellite-based active and passive measurements, sampling of the inner TC core and the interaction with the storm environment is becoming well observed.

Wind shear has been extensively documented as having an influence on TC formation and intensification (Thatcher and Zhaoxia 2011 and references therein) and predictability (Zhang and Tao 2013). For our work vertical wind shear is defined as the difference between 200- and 850-hPa winds from the storm center to 500 km and is calculated from global GFS analysis fields at 1° resolution. The difference in winds between 200 and 850 hPa is selected because TC systems are highly impacted by the mass-weighted flow differences in this region, and this value is a common wind shear criterion cited throughout previous literature.

Early work on the effects of vertical wind shear on TC intensity began with a venting hypothesis (Gray 1968) by advection of warmer upper-level air from the center of the storm. Larger values of wind shear can inhibit TC formation by carrying away the heating in the upper troposphere from the lower-level circulation, thus tearing apart the system, disrupting further formation, and increasing the storm's central pressure. The importance of the tilting of the vortex is explored by Shapiro (1992), Flatau et al. (1994), and Wang and Holland (1996). The upper- and lower-level vortex can become uncoupled with the upper-level vortex experiencing a large degree of tilt correlated with the magnitude and strength of the wind shear, weakening the system.

DeMaria (1996) hypothesized wind shear changes the thermal structure of the storm. Displacement of upper and lower vortex environments causes a thermal structure shift downshear, resulting in a temperature change and disrupting storm circulation.

Wind shear simulations from MM5 demonstrate changes of TC intensity and evolution (Frank and Ritchie 2001) with results revealing upper-level circulation weakening from the top downward as a consequence of changes in the positioning of potential vorticity venting out of

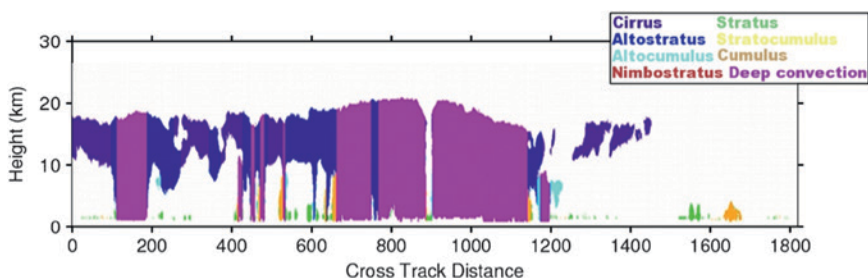
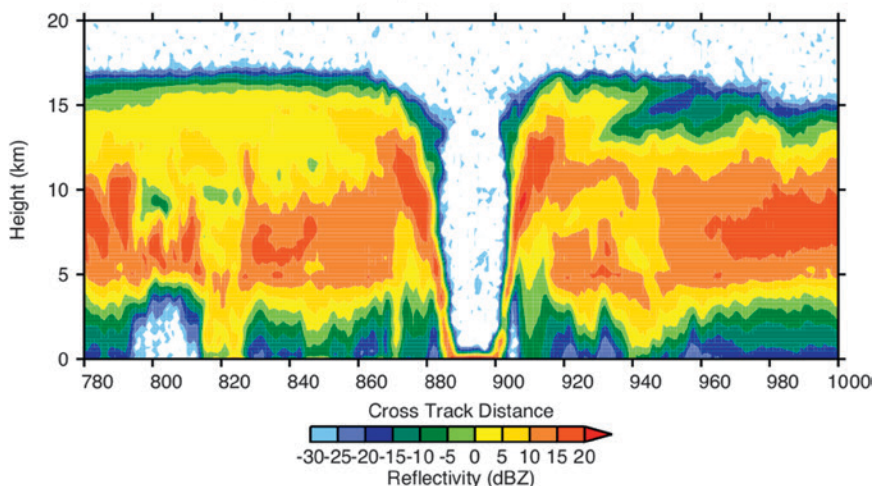


FIG. 6. CS cloud classification of Typhoon Choi-Wan on 0352 UTC 15 Sep 2009.

the core of the TC system. Observations of temperature soundings from AMSU found as wind shear increases, the warm core erodes downward from fluxes of potential temperatures, but details of how this occurs and effects on the TC inner core are lacking (Knaff et al. 2004). More recent observational studies using airborne Doppler radar composites of HTC-strength storms (Reasor et al. 2013) confirms the impact of shear forcing in the direction of the large-scale shear, but the magnitude of the tilt does not show a relationship to the intensity of the vertical wind shear. Tang and Emanuel (2012) modeled the sensitivity of TCs to ventilation of cooler, drier air into the inner core using an axisymmetric TC. Ventilation at the midlevels was the most effective at reducing the intensity of a TC, while upper-level ventilation did not appear to have much of a weakening effect.

Using over-ocean CS CPR reflectivity observations, TC reflectivity profiles are stratified with respect to varying degrees of wind shear and are examined as a function of radial distance from storm center. In this study, reflectivity and height profiles are averaged from 0 to 300 km from the TC storm center. Reflectivity profiles (and corresponding heights) are grouped according to radial distance (0–300 km) in bins of 2 km. All reflectivity profile points between 0 and 2, 2 and 4, 4 and 6 km, and so forth from the storm center are grouped together according to bin size and height. A 2-km bin size provides decent resolution of areas in a TC; larger bin sizes tend to smooth out the finer core details. The array of grouped reflectivity data are inverse base 10 log averaged (heights are averaged) to produce a smaller array of average reflectivity array at each bin size as a function of average height.

(a) Reflectivity CHOI-WAN-9/15/2009



(b) Reflectivity CHOI-WAN-9/15/2009

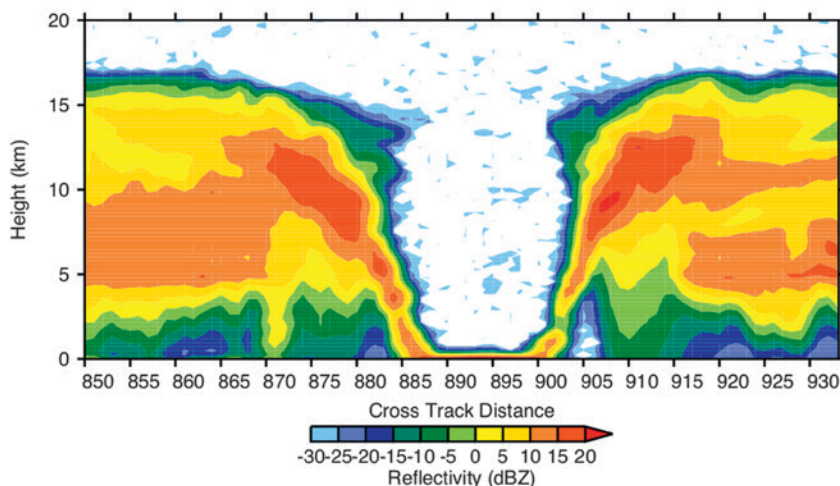


FIG. 7. (a) Zoomed-in eye portion of Typhoon Choi-Wan at 0352 UTC 15 Sep 2009. (b) One-to-one aspect ratio of the eye portion.

A total of 3,988 TC overpasses with winds greater than 10.3 m s^{-1} and SST storm center $\geq 26.0^\circ\text{C}$ during the period 2 June 2006–31 December 2013 are analyzed into three equal composites containing low wind shear (less than 5.1 m s^{-1}), moderate wind shear (between 5.1 and 8.9 m s^{-1}), and high wind shear (greater than 8.9 m s^{-1}) (Fig. 8). The mean value of this distribution set is 7.7 m s^{-1} with a standard deviation of 4.6 m s^{-1} ; the distribution is skewed toward lower values of wind shear. Examination of Fig. 8 shows moderate wind shear has the largest impact on the vertical convective cores (10 dbZ). The vertical size is limited to less than 10 km with CTHs peaking at 75 km from storm center. Interestingly, shear values $\geq 8.9 \text{ m s}^{-1}$ produce 10-dbZ convective core heights over 15 km tall 25 km from storm center. Overall, CTHs in the first 20 km from storm center decrease substantially, but higher wind shear does not have as much of an impact on

the vertical height of the vertical convective cores. Low wind shear produces a more uniform average reflectivity with 10-dBZ cores decreasing in vertical size as the distance from the storm center increases. Overall examination of these results reveals increasing wind shear displacing vertical cores farther from the storm center and decreasing CTHs, most notably in the first 25 km. This supports the theory of upper-level

weakening with convection being pushed outward away from the storm center.

However, examining the effects of wind shear on HTC-strength storms appears to have a more substantial effect on the structure of these storms (Fig. 9). A total of 1,007 TC profiles with SST storm center $\geq 26^{\circ}\text{C}$ are collected during the same period of 2 June 2006–31 December 2013 and similarly

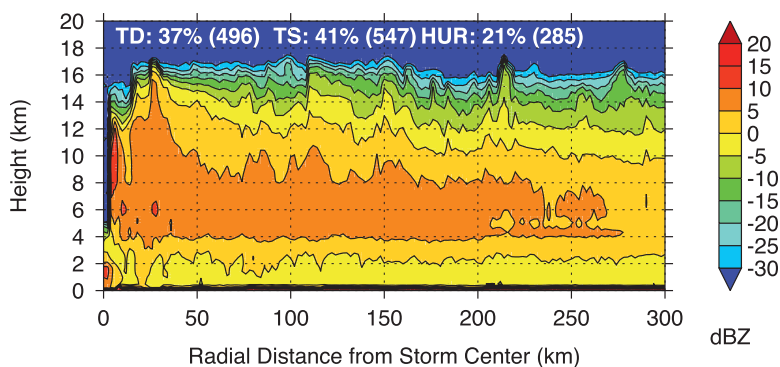
analyzed into three equal composites of low wind shear (less than 4.5 m s^{-1}), moderate wind shear (between 4.5 and 8.4 m s^{-1}), and high wind shear (greater than 8.4 m s^{-1}). The mean value of this distribution set is 7.1 m s^{-1} with a standard deviation of 4.3 m s^{-1} also skewing the distribution toward lower values of wind shear. High wind shear limits convective cores (10 dBZ) to less than 10 km in vertical height in the first 100 km from storm center and pushes these areas farther from the storm center (where the convective cores peak at 12 km in height at 125 km). CTHs peak at 40 km from the storm center with a vertical height of just over 16 km. Moderate wind shear has very little effect on the structure of the TC; in fact, this composite contains larger, 10 dBZ, cores and larger average CTHs than that of low or high wind shear composites. This supports previous studies that report that some amount of wind shear is not always detrimental to a storm system and that it can actually act to enhance convective cores (Tuleya and Kurihara 1981; Paterson et al. 2005). The 10-dBZ convective cores in low wind shear peak at over 15 km in vertical height much farther from the storm center at 30 km. The low wind shear regime is very disorganized in the first 30 km, but it could also be a consequence of increased sampling of TCs with large eyes.

High values of wind shear are observed more often in storms of the ATL basin, where a higher quantity of storms are observed (73 cases) due to the greater latitudinal extent of the ATL basin in the midlatitudes.

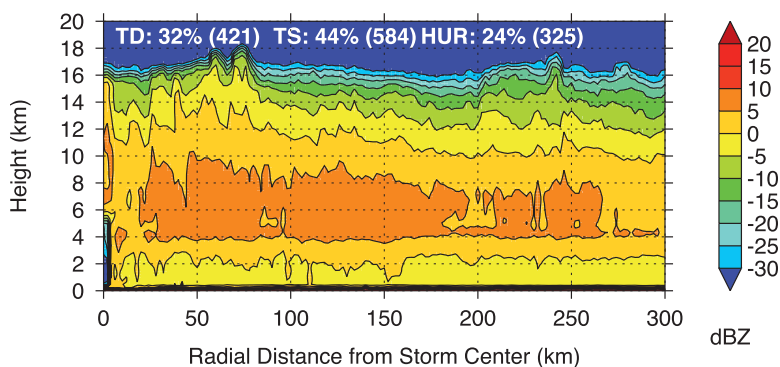
Average Reflectivity by Shear (m/s)

Winds GE 10.3 m/s & SST GE 26.0 C

Shear GT 8.9 - 1328 cases



Shear GT 5.1 and LE 8.9 - 1330 cases



Shear LE 5.1 - 1330 cases

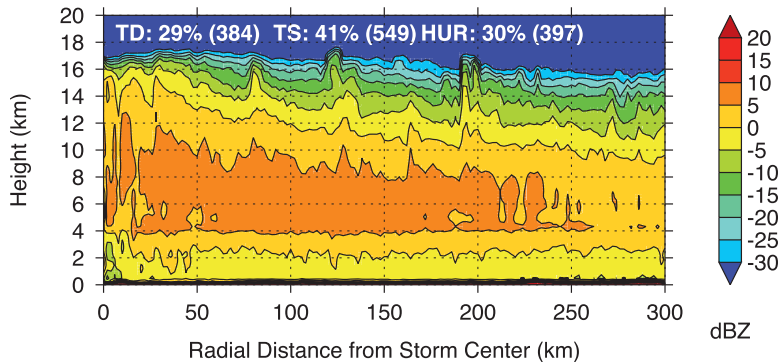


FIG. 8. Average reflectivity stratified by varying wind shear (200–850 hPa) of tropical systems with winds greater than 10.3 m s^{-1} and SST $\geq 26.0^{\circ}\text{C}$. Percentage of storms classified by strength (TD, TS, HTC) for the period 2 Jun 2006–31 Dec 2013.

In contrast, the EPAC basin is more heavily distributed with TC composites in lower shear cases (59 cases), as storms moving poleward tend to weaken due to cooler SSTs and entrainment of dry air.

Compositing CS CPR reflectivity observations for TCs reveal that as wind shear increases, CTHs decrease and convective cores shift outward from the storm center, supporting the theory of upper-level weakening and a shifting of convective cores from the storm center. The convective cores do not necessarily weaken in size as evident in Fig. 8; high shear for TDs, TSs, and HTCs limits CTHs in the first 20 km, but an increase in wind shear tends to shift these convective bursts farther from the storm center. For HTC-strength storms, moderate wind shear shows the most favorable storm structure, with increasing wind shear shifting convective cores farther from the storm center and suppressing convective cores to less than 10 km in vertical height. CTHs are notably lower in the first 30 km from the storm center of HTC-strength storm systems as wind shear increases. Future work will examine TC reflectivity composites relative to the direction of the large-scale shear, examining the effects of wind shear on weakening and strengthening storm systems and wind shear at varying tropospheric levels.

CONCLUSIONS. The CS TC dataset is a first-of-its-kind compilation of A-Train satellite observations and model data from CS CPR intersects of global TC systems. While information about individual storms is sparse, the CS TC dataset provides a rich composite of information that can establish an important new framework for studying these systems where ground and aircraft measurement can prove elusive. This one-of-a-kind dataset provides detailed information on vertical cloud layers, precipitation structure, cloud properties, convective cores, environmental storm conditions, and best-track data of global TCs. These

unique observations and measurements provide an additional data source for validation of passive radiometers and numerical models along with first-time spaceborne microwave satellite observations of the inner vertical details of TCs. We illustrate the value of compositing data with respect to environmental

Average Reflectivity by Shear (m/s)

Winds GE 33.0 m/s & SST GE 26.0 C

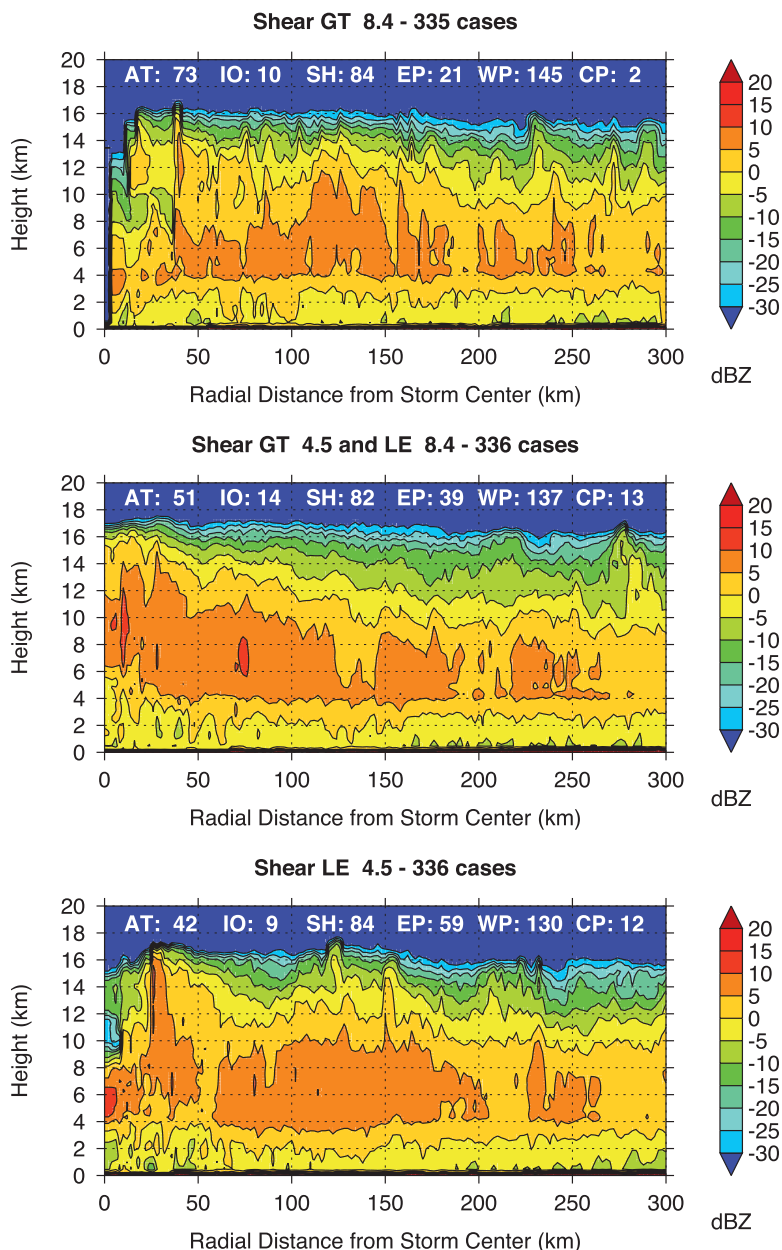


FIG. 9. Average reflectivity stratified by wind shear (200–850 hPa) of tropical systems with winds greater than 33.0 m s⁻¹ and SST ≥ 26.0°C (HTC strength). Total overpasses for storms in the Atlantic (AT), Indian Ocean (IO), Southern Hemisphere (SH), east Pacific (EP), west Pacific (WP), and central Pacific (CP) areas are identified. Observations for the period 2 Jun 2006–31 Dec 2013.

conditions with the example of wind shear. Compositing CPR reflectivity profiles as a function of wind shear clearly reveals the extent wind shear influences the structure of TCs. Mature HTC-strength storms are more susceptible to the influence of stronger wind shear than weaker TD- or TS-strength storms, and moderate values of wind shear tend to show favorable storm structure. Higher values of wind shear on HTC-strength storms push the convective cores away from the storm center and limit CTHs.

ACKNOWLEDGMENTS. We would like to acknowledge the Satellite Meteorological Applications Section at the Naval Research Laboratory for its assistance in creating the TC composites and the CS DPC for supplying the data used throughout this study. Special thanks to Cristian Mistrescu, Kim Richardson, and Steve Miller for their assistance on this project. Special thanks to John Knaff and two anonymous reviewers for their thoughtful and helpful feedback. This project is funded under NASA JPL Contract 1439268.

APPENDIX: SUMMARY OF ACRONYMS.

AIRS	Atmospheric Infrared Sounder
AMSR-E	Advanced Microwave Scanning Radiometer for Earth Observing System
AMSU	Advanced Microwave Sounding Unit
ATCF	Automated Tropical Cyclone Forecasting System
ATL	Atlantic
A-Train	Afternoon satellite constellation
CALIOP	Cloud–Aerosol Lidar with Orthogonal Polarization
CALIPSO	<i>Cloud–Aerosol Lidar and Infrared Pathfinder Satellite Observations</i>
CERES	Clouds and the Earth’s Radiant Energy System
CPAC	Central Pacific
CPHC	Central Pacific Hurricane Center
CPR	Cloud Profiling Radar
CS	<i>CloudSat</i>
CTH	Cloud-top height
CTT	Cloud-top temperature
DPC	Data Processing Center
ECMWF	European Centre for Medium-Range Weather Forecasts
EPAC	Eastern Pacific
GFS	Global Forecast System
HDF-EOS	Hierarchical data format–Earth Observing System
HTC	Hurricane/tropical cyclone/cyclone
IO	Indian Ocean
IWC	Ice water content
IWP	Ice water path
JTWC	Joint Typhoon Warning Center
MLS	Microwave Limb Sounder
MM5	Fifth-generation Pennsylvania State University–National Center for Atmospheric Research Mesoscale Model
MODIS	Moderate Resolution Image Spectroradiometer
NAVEM	Navy Global Environmental Model
NHC	National Hurricane Center
NOGAPS	Navy Operational Global Atmospheric Prediction System
NRL	Naval Research Laboratory
SST	Sea surface temperature
SHEM	Southern Hemisphere
TC	Tropical cyclone
TD	Tropical depression
TS	Tropical storm
WMO	World Meteorological Organization
WPAC	Western Pacific
YOTC	Year of the Tropical Convection

REFERENCES

- Barnes, G. M., E. J. Zipser, D. Jorgensen, and F. Marks Jr, 1983: Mesoscale and convective structure of a hurricane rainband. *J. Atmos. Sci.*, **40**, 2125–2137, doi:10.1175/1520-0469(1983)040<2125:MACSOA>2.0.CO;2.
- Black, M., J. Gamache, F. Marks, C. Samsury, and H. Willoughby, 2002: Eastern Pacific Hurricanes Jimena of 1991 and Olivia of 1994: The effect of vertical shear on structure and intensity. *Mon. Wea. Rev.*, **130**, 2291–2312, doi:10.1175/1520-0493(2002)130<2291:EPHJOA>2.0.CO;2.
- Camp, J. P., and M. T. Montgomery, 2001: Hurricane maximum intensity: Past and present. *Mon. Wea. Rev.*, **129**, 1704–1717, doi:10.1175/1520-0493(2001)129<1704:HMPAP>2.0.CO;2.
- EMC, 2003: The GFS atmospheric model. NCEP Office Note 442, 14 pp.
- DeMaria, M., 1996: The effect of vertical shear on tropical cyclone intensity change. *J. Atmos. Sci.*, **53**, 2076–2088, doi:10.1175/1520-0469(1996)053<2076:TEOVSO>2.0.CO;2.
- Dvorak, V. F., 1972: A technique for the analysis and forecasting of tropical cyclone intensities from satellite pictures. NOAA Tech. Memo. NESS 36, 15 pp. [Available from NOAA/NESDIS, 5200 Auth Rd., Washington, DC 20333.]
- , 1975: Tropical cyclone intensity analysis and forecasting from satellite imagery. *Mon. Wea. Rev.*, **103**, 420–430, doi:10.1175/1520-0493(1975)103<0420:TCIAAF>2.0.CO;2.
- , 1984: Tropical cyclone intensity analysis using satellite data. NOAA Tech Rep. 11, 45 pp. [Available from NOAA/NESDIS, 5200 Auth Rd., Washington, DC 20333.]
- Ellis, T. D., T. L'Ecuyer, J. Haynes, and G. Stephens, 2009: How often does it rain over the global oceans? The perspective from CloudSat. *Geophys. Res. Lett.*, **36**, L03815, doi:10.1029/2008GL036728.
- Flatau, M., W. H. Schubert, and D. E. Stevens, 1994: The role of baroclinic processes in tropical cyclone motion: The influence of vertical tilt. *J. Atmos. Sci.*, **51**, 2589–2601, doi:10.1175/1520-0469(1994)051<2589:TROBPI>2.0.CO;2.
- Frank, W. M., and E. A. Ritchie, 2001: Effects of vertical wind shear on the intensity and structure of numerically simulated hurricanes. *Mon. Wea. Rev.*, **129**, 2249–2269, doi:10.1175/1520-0493(2001)129<2249:EOVWSO>2.0.CO;2.
- Gray, W. M., 1968: Global view of the origin of tropical disturbances and storms. *Mon. Wea. Rev.*, **96**, 669–700, doi:10.1175/1520-0493(1968)096<0669:GVOTOO>2.0.CO;2.
- Guimond, S. R., G. M. Heymsfield, and F. J. Turk, 2010: Multiscale observations of Hurricane Dennis (2005): The effects of hot towers on rapid intensification. *J. Atmos. Sci.*, **67**, 633–654, doi:10.1175/2009JAS3119.1.
- Haynes, J. M., T. H. V. Haar, T. L'Ecuyer, and D. Henderson, 2013: Radiative heating characteristics of Earth's cloudy atmosphere from vertically resolved active sensors. *Geophys. Res. Lett.*, **40**, 624–630, doi:10.1002/grl.50145.
- Hogan, T., and T. Rosmond, 1991: The description of the Navy Operational Global Atmospheric Prediction System's spectral forecast model. *Mon. Wea. Rev.*, **119**, 1786–1815, doi:10.1175/1520-0493(1991)119<1786:TDOTNO>2.0.CO;2.
- Houze, R., Jr., and Coauthors, 2006: The hurricane rainband and intensity change experiment: Observations and modeling of Hurricanes Katrina, Ophelia, and Rita. *Bull. Amer. Meteor. Soc.*, **87**, 1503–1521, doi:10.1175/BAMS-87-11-1503.
- Jin, Y., and Coauthors, 2014: The impact of ice phase cloud parameterizations on tropical cyclone prediction. *Mon. Wea. Rev.*, **142**, 606–625, doi:10.1175/MWR-D-13-00058.1.
- Kidder, S. Q., and T. H. Vonder Haar, 1995: *Satellite Meteorology: An Introduction*. International Geophysics Series, Vol. 1, Academic Press, 466 pp.
- Knaff, J. A., S. A. Seseske, M. DeMaria, and J. L. Demuth, 2004: On the influences of vertical wind shear on symmetric tropical cyclone structure derived from AMSU. *Mon. Wea. Rev.*, **132**, 2503–2510, doi:10.1175/1520-0493(2004)132<2503:OTIOVW>2.0.CO;2.
- Luo, Z., G. L. Stephens, K. A. Emanuel, D. G. Vane, N. D. Tourville, and J. M. Haynes, 2008: On the use of CloudSat and MODIS data for estimating hurricane intensity. *IEEE Geosci. Remote Sens. Lett.*, **5**, 13–16, doi:10.1109/LGRS.2007.905341.
- Mace, G. G., Q. Zhang, M. Vaughan, R. Marchand, G. Stephens, C. Trepte, and D. Winker, 2009: A description of hydrometeor layer occurrence statistics derived from the first year of merged CloudSat and CALIPSO data. *J. Geophys. Res.*, **114**, D00A26, doi:10.1029/2007JD009755.
- Mitrescu, C., S. Miller, G. Hawkins, T. L. Ecuyer, J. Turk, P. Partain, and G. Stephens, 2008: Near-real-time applications of CloudSat data. *J. Appl. Meteor. Climatol.*, **47**, 1982–1994, doi:10.1175/2007JAMC1794.1.
- Montgomery, M. T., M. E. Nicholls, T. A. Cram, and A. B. Saunders, 2006: A vortical hot tower route to tropical cyclogenesis. *J. Atmos. Sci.*, **63**, 355–386, doi:10.1175/JAS3604.1.
- Nayak, M., M. Witkowski, D. Vane, T. Livermore, and M. Rokey, 2012: CloudSat anomaly recovery and

- operational lessons learned. *Proc. 12th Int. Conf. on Space Operations*, Stockholm, Sweden, CNES, Paper 1295798. [Available online at www.spaceops2012.org/proceedings/documents/id1295798-Paper-001.pdf.]
- Paterson, L. A., B. N. Hanstrum, N. E. Davidson, and H. C. Weber, 2005: Influence of environmental vertical wind shear on the intensity of hurricane-strength tropical cyclones in the Australian region. *Mon. Wea. Rev.*, **133**, 3644–3660, doi:10.1175/MWR3041.1.
- Reasor, P. D., R. Rogers, and S. Lorsolo, 2013: Environmental flow impacts on tropical cyclone structure diagnosed from airborne Doppler radar composites. *Mon. Wea. Rev.*, **141**, 2949–2969, doi:10.1175/MWR-D-12-00334.1.
- Reynolds, R. W., T. M. Smith, C. Liu, D. B. Chelton, K. S. Casey, and M. G. Schlax, 2007: Daily high-resolution-blended analyses for sea surface temperature. *J. Climate*, **20**, 5473–5496, doi:10.1175/2007JCLI1824.1.
- Riehl, H., and J. S. Malkus, 1958: On the heat balance in the equatorial trough zone. *Geophysica*, **6**, 503–538.
- Sampson, C., and A. J. Schrader, 2000: The Automated Tropical Cyclone Forecasting System (version 3.2). *Bull. Amer. Meteor. Soc.*, **81**, 1231–1240, doi:10.1175/1520-0477(2000)081<1231:TATCFS>2.3.CO;2.
- Sassen, K., Z. Wang, and D. Liu, 2009: Cirrus clouds and deep convection in the tropics: Insights from CALIPSO and CloudSat. *J. Geophys. Res.*, **114**, D00H06, doi:10.1029/2009JD011916.
- Shapiro, L. J., 1992: Hurricane vortex motion and evolution in a three-layer model. *J. Atmos. Sci.*, **49**, 140–153, doi:10.1175/1520-0469(1992)049<0140:HVM AEI>2.0.CO;2.
- Stephens, G. L., and Coauthors, 2002: The CloudSat mission and the A-train. *Bull. Amer. Meteor. Soc.*, **83**, 1771–1790, doi:10.1175/BAMS-83-12-1771.
- , and Coauthors, 2008: CloudSat mission: Performance and early science after the first year of operation. *J. Geophys. Res.*, **113**, D00A18, doi:10.1029/2008JD009982.
- , and Coauthors, 2012: An update on Earth’s energy balance in light of the latest global observations. *Nat. Geosci.*, **5**, 691–696, doi:10.1038/ngeo1580.
- Tang, B., and K. Emanuel, 2012: A ventilation index for tropical cyclones. *Bull. Amer. Meteor. Soc.*, **93**, 1901–1912, doi:10.1175/BAMS-D-11-00165.1.
- Thatcher, L., and P. Zhaoxia, 2011: How vertical wind shear affects tropical cyclone intensity change: An overview. *Recent Hurricane Research—Climate, Dynamics, and Societal Impacts*, A. Lupo, Ed., InTech, 269–286.
- Tuleya, R. E., and Y. Kurihara, 1981: A numerical study on the effects of environmental flow on tropical storm genesis. *Mon. Wea. Rev.*, **109**, 2487–2506, doi:10.1175/1520-0493(1981)109<2487:ANSOTE>2.CO;2.
- Uppala, S. M., and Coauthors, 2005: The ERA-40 Re-Analysis. *Quart. J. Roy. Meteor. Soc.*, **131**, 2961–3012, doi:10.1256/qj.04.176.
- Waliser, D. E., and Coauthors, 2012: The “year” of tropical convection (May 2008 to April 2010): Climate variability and weather highlights. *Bull. Amer. Meteor. Soc.*, **93**, 1189–1218, doi:10.1175/2011BAMS3095.1
- Wang, Y., and G. J. Holland, 1996: Tropical cyclone motion and evolution in vertical shear. *J. Atmos. Sci.*, **53**, 3313–3332, doi:10.1175/1520-0469(1996)053<3313:TCMAEI>2.0.CO;2.
- Zhang, F., and D. Tao, 2013: Effects of vertical wind shear on the predictability of tropical cyclones. *J. Atmos. Sci.*, **70**, 975–983, doi:10.1175/JAS-D-12-0133.1.